Global mean sea surface and marine gravity anomaly from multi-satellite altimetry: applications of deflection-geoid and inverse Vening Meinesz formulae

C. Hwang, H.-Y. Hsu, R.-J. Jang

Department of Civil Engineering, National Chiao Tung University, 1001 Ta Hsueh Road,
Hsinchu 300, Taiwan; e-mail: hwang@geodesy.cv.nctu.edu.tw; Tel.: +886-3-5724739; Fax: +886-3-5716257

Abstract. Global mean sea surface heights (SSHs) and gravity anomalies on a $2' \times 2'$ grid were determined from Seasat, Geosat (Exact Repeat Mission and Geodetic Mission), ERS-1 (1.5-year mean of 35-day, and GM), TOPEX/POSEIDON (T/P) (5.6-year mean) and ERS-2 (2-year mean) altimeter data over the region $0°$–$360°$ longitude and $-80°$–$80°$ latitude. To reduce ocean variabilities and data noises, SSHs from non-repeat missions were filtered by Gaussian filters of various wavelengths. A Levitus oceanic dynamic topography was subtracted from the altimeter-derived SSHs, and the resulting heights were used to compute along-track deflection of the vertical (DOV). Geoidal heights and gravity anomalies were then computed from DOV using the deflection-geoid and inverse Vening Meinesz formulae. The Levitus oceanic dynamic topography was added back to the geoidal heights to obtain a preliminary sea surface grid. The difference between the T/P mean sea surface and the preliminary sea surface was computed on a grid by a minimum curvature method and then was added to the preliminary grid. The comparison of the NCTU01 mean sea surface height (MSSH) with the T/P and the ERS-1 MSSH result in overall root-mean-square (RMS) differences of 5.0 and 3.1 cm in SSH, respectively, and 7.1 and 3.2 µrad in SSH gradient, respectively. The RMS differences between the predicted and shipborne gravity anomalies range from 3.0 to 13.4 mGal in 12 areas of the world's oceans.

Keywords: Mean sea surface – Gravity anomaly – Altimetry – Deflection geoid – Inverse Vening Meinesz

1 Introduction

Satellite altimetry has opened a new era in Earth sciences research. A recent compilation of satellite altimetry applications can be found in Fu and Cazenave (2001). Mean sea surface height (MSSH) and marine gravity anomaly are the most two important products of satellite altimetry for geodetic and geophysical applications. MSSH is useful in numerous applications, such as global tide modeling, sea-level-change study, reduction of altimeter observations to reference tracks, and bathymetry prediction. Applications of marine gravity have been illustrated in e.g. Sandwell and Smith (1997). Disregarding the sea surface topography (SST), marine gravity anomaly is basically equivalent to MSSH, and the two have a simple, linear relationship in the spectral domain. Current global MSSH models have been largely constructed by direct gridding of altimeter observed sea surface heights (SSHs), e.g. the MSSH models of Kort-og Matrikelstyrelsen (KMS) (Andersen and Knudsen 1998), the National Aeronautics and Space Administration (NASA)/Goddard Space Flight Center (GSFC) (Wang 2000), and Collecte Localisation Satellites (CLS) (Hernandez and Schaeffer 2000). A somewhat unconventional approach was employed by Yi (1995), who used a combined SSH and geoid gradient from multi-satellite missions to construct the OSU95 MSSH model see also Rapp and Yi (1997). When using the direct gridding method, SSHs must be carefully crossover adjusted to remove inconsistency of SSHs at crossover points. Insufficient or improper crossover points will easily lead to artifacts in the resulting field, such as track pattern and extremely large signature. With MSSH computed, marine gravity anomaly can be obtained by a simple conversion in the spectral domain, see e.g. Schwarz et al. (1990) for a complete derivation of the spectral conversion between MSSH and gravity anomaly (assuming that SST is removed).

A completely different approach to gravity anomaly recovery from satellite altimetry data uses deflections of the vertical (DOV) as the data type. The major argument of using DOV is that DOV are less contaminated by long-wavelength errors than SSH, and using DOV requires no crossover adjustment; see e.g. Sandwell and Smith (1997), Hwang et al. (1998), and Andersen and

---

Correspondence to: C. Hwang

Knudsen (1998). With DOV from altimetry, it is possible to compute MSSH using the deflection-geoid formula derived by Hwang (1998). Taking the advantage of DOV, in this paper we will compute simultaneously a global MSSH grid and a global gravity anomaly grid using the deflection geoid and the inverse Vening Meinesz formulae from multi-satellite altimetry data. Running in parallel to this study is a complete update of the altimeter database in our research institute, incorporating the most recent geophysical data records (GDRs), and the latest models of ocean tide and other geophysical corrections. Many tests for optimal parameters of computations will be performed in the South China Sea (SCS), which covers coastal areas, continental shelf, and areas of median and great depth. The location of the SCS and its gravity signature can be found in Hwang (1998).

2 Multi-satellite altimeter data and processing

2.1 Description of altimeter data sets

Table 1 lists the altimeter data used in computing the global MSSH and gravity anomaly grids. The data are from five satellite missions and span more than 20 years. The Seasat data are from the Ohio State University and are edited by Liang (1983), who have also crossover-adjusted the Seasat orbits. The Geosat data are from the National Oceanic and Atmospheric Administration (NOAA) and contain the latest JGM3 orbits and geophysical correction models (NOAA 1997). In the Geosat/GM JGM3 GDRs, the wet and dry troposphere corrections are based on the models of the National Centers for Environmental Prediction (NCEP)/National Center for Atmospheric Research (NCAR) (Kalnay et al. 1996) and the NASA Water Vapor Project (NVAP) (Randel et al. 1996), and the ionosphere correction is adopted from the IRI95 model (Bilitza 1997). The sea-state bias, which introduces an error to the measured range, is also recomputed and is more accurate than the previous version of GDRs. The ERS-1 and ERS-2 data are from the Centre ERS d'Archivage et de Traitement (CERSAT) France, and their orbits have been adjusted to the TOPEX/POSEIDON (T/P) orbits by Le Traon and Ogor (1998). Finally, the T/P data are provided by Archiving, Validation, and Interpretation of Satellite Oceanographic Data (AVISO) (1996), and should have the best point data quality among all altimeter data, due to low altimeter noise and state-of-the-art orbit and geophysical correction models.

The Geosat/GM and ERM GDRs from the NOAA contain both raw measurements at 10 samples per second (10 Hz) and the 1-s averaged SSH. To increase spatial resolution, we re-processed the raw data to obtain SSHs at two samples per second. When re-sampling, the 10-Hz SSHs were first approximated by a second-degree polynomial and the desired two-per-second (2-Hz) SSHs were then computed from the solve-for polynomial coefficients. Pope's (1976) tau-test procedure was used to screen any erroneous raw data. Among these data sets, Geosat/GM and ERS-1/GM have very high 2-D spatial density and will contribute most to the high-frequency parts of MSSH and gravity fields. In one test over the SCS we used separately the new JGM3 and the old T2 versions of Geosat/GM altimeter data to predict gravity anomalies and it was found that the RMS differences between the predicted and shipborne gravity anomalies were 10.65 and 9.77 mGal, respectively. Thus the JGM3 version indeed outperforms the T2 version.

2.2 Averaging SSH: variability and noise of SSH

The altimeter data from the repeat missions (Geosat/ERM, ERS-1/35d, ERS-2/35d, and T/P) were averaged to reduce time variability and data noise. When averaging, Pope's tau-test procedure was also employed to eliminate erroneous observations (Pope 1976). However, it turns out that the Geosat observed SSHs behave erratically (for example, large jumps of SSHs an along-track observations) and Pope's method failed to detect outlier SSHs on several occasions. Thus for Geosat/ERM a modified averaging/outlier rejection procedure was used. In this new procedure, at any locations, SSHs from repeat cycles are first sorted to find the median value. Then, the difference between individual SSHs and the median is computed. Any SSH with difference larger than 0.45 m is flagged as an outlier and removed (0.45 m is based on three times the point standard deviation of Geosat/ERM; see below). The desired MSSH is finally computed from the cleaned SSH by simple averaging. Table 2 lists the statistics associated with the averaged and non-averaged SSHs. For the repeat missions in Table 2, we computed the point standard deviation (SD) of SSH as

Table 1. Satellite altimeter missions and data used for the global computation

Mission	Repeat period (days)	Data duration	Orbit height (km)	Inclination angle (°)	Mean track separation at the equator (km)
Seasat	no	78/08–78/11	780	108	165
Geosat/GM	no	85/03–86/09	788	108	4
Geosat/ERM	17	86/11–90/01	788	108	165
ERS1-/35d	35	92/04–93/12 95/03–96/06	781	98.5	80
ERS-1/GM	no	94/04–95/03	781	98.5	8
ERS-2/35d	35	95/04–98/10	785	98.5	80
T/P	10	92/12–00/06	1336	66	280

Table 2. Statistics of SSHs from seven satellite altimeter missions

Mission	No. repeat cycles	No. passes	No. points	No. points in deep ocean[a]	Averaged SD of SSH[b] (m)
Seasat	no	3314	1 269 169	6419	–
Geosat/GM	no	15 708	25 530 238	151 044	0.141
Geosat/ERM	68	488	1 991 672	4798	0.026
ERS1-/35d	26	1002	1 677 190	4805	0.023
ERS-1/GM	no	9532	14 702 377	44 928	–
ERS-2/35d	37	1002	1 141 786	4815	0.022
T/P	239	254	553 525	1387	0.009

[a] Over the area 25°S–15°S and 235°E–245°E where there is no land
[b] The SD of Geosat/GM is the SD of 2-Hz SSHs from fitting the 10-Hz SSHs

$$\sigma_h(i,j) = \sqrt{\frac{\sum_{k=1}^{n}(h(i,j,k) - \bar{h}(i,j))^2}{n-1}} \qquad (1)$$

where $h(i,j)$ is the observed SSH at point i along pass j, $\bar{h}(i,j)$ is the averaged SSH and n is the number of points. According to statistical theory, the SD of averaged height $\bar{h}(i,j)$ is

$$\sigma_{\bar{h}}(i,j) = \frac{\sigma_h(i,j)}{\sqrt{n}} \qquad (2)$$

Thus the accuracy increases with number of repeat cycles. A point SD can be expressed as

$$\sigma_h = \sqrt{\sigma_i^2 + \sigma_o^2 + \sigma_g^2 + \sigma_s^2} \qquad (3)$$

where

σ_i = instrument error (random part + time-dependent part)

σ_o = orbit error (random part + non-geographical correlated error)

σ_g = errors in geophysical correction models (random + systematic errors)

σ_s = sea surface variability (excluding tidal variation)

In Eq. (3) it is assumed that the various factors are uncorrelated. Thus, a point SD contains both random noises and variabilities arising from a variety of sources. Figure 1 shows the point SDs derived by averaging Geosat/ERM, ERS-1/35d, and T/P (ERS-2/35d SD is close to ERS-1/35d SD, so it is not shown here). Clearly the SDs from the three repeat missions have the same patterns of distribution. Over oceanic areas of high variability, such as the Kuroshio Extension, the Gulf Stream, the Brazil Current, the Agullas Current, and the Antarctic Circumpolar Currents, sea surface variability contributes most to SD. SD is also relatively high in the tropics and the western Pacific areas, where meso-scale eddies are very active. Clearly, the pattern of sea surface variability has been very stable over the past two decades, as the Geosat/ERM-derived SDs in the 1980s and the ERS-1 and T/P-derived SDs in the 1990s show very consistent signature. In the polar regions (above ±67°), SD will be less reliable because of ice contamination and sparse data samples. Over shallow waters, tide model error becomes dominant in SD and is particularly pronounced in the continental shelves of the western Pacific, northern Europe, and eastern Australia. In the immediate vicinity of coasts, the interference of altimeter waveforms by landmass further increases SD. Over the deep, quiet oceans, SD is in general very small and here along-track MSSH will be best determined. Note that in Table 2 the SD of Geosat/GM is simply the SD of the 2-Hz SSHs as derived from the fitting of the 10-Hz SSHs, so it does not represent the noise level of 2-Hz SSHs.
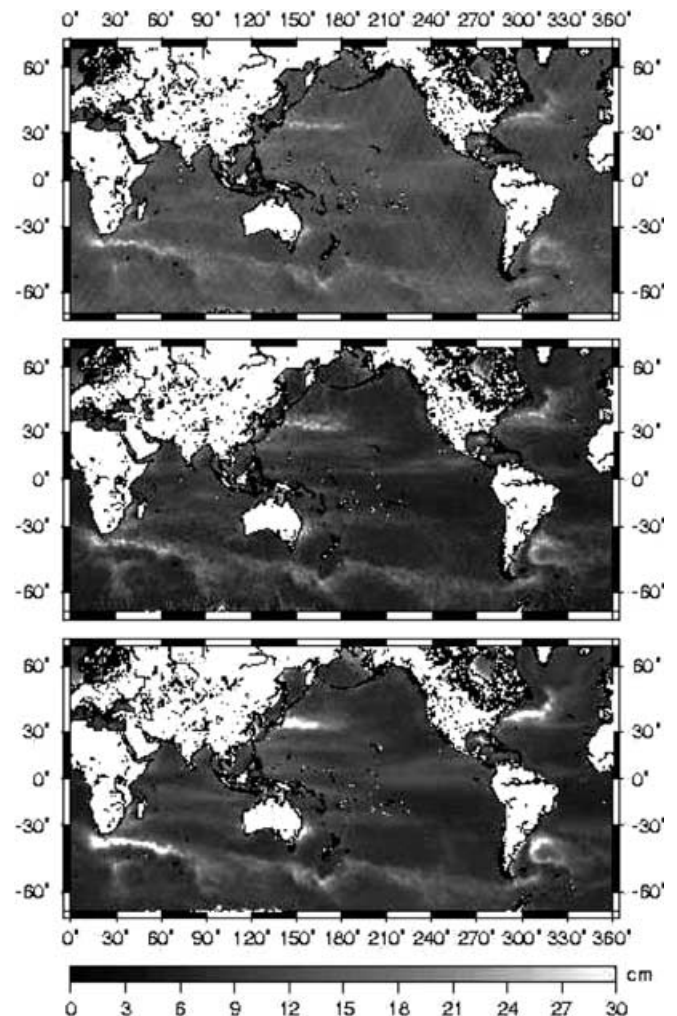

Fig. 1. Estimated standard deviations of point SSHs of Geosat/ERM (top), ERS-1 (center) and TOPEX/POSEIDON (bottom)

The SD of SSH will be used in deriving the SD of along-track DOV, which in turn will be used in gridding DOV components by least-squares collocation (LSC) (see below). Due to the complex factors listed in Eq. (3), it will be difficult to estimate the SD of SSH for the non-repeat missions. For the purpose of computing MSSH and gravity grids, we could model the covariance function of ocean variability as in Andersen and Knudsen (1998), or reduce the ocean variability by filtering as in Hwang et al. (1998). A detailed analysis of the effect of ocean variability on MSSH and gravity recovery from altimetry can be found in Rapp and Yi (1997).

2.3 Choice of ocean tide model

The ocean tide creates a deviation of the instantaneous sea surface from the mean sea surface. There are now more than 10 global ocean tide models available for correcting tidal effect in altimetry (Shum et al. 1997). Table 3, partly from Matsumoto et al. (2000), shows the RMS collinear differences of T/P and the errors in along-track DOV using NAO99b (Matsumoto et al. 2000), CSR4.0 (Eanes 1999), and GOT99.2b (Matsumoto et al. 2001) tide models. Both NAO99b and GOT99.2b are based on hydrodynamic solutions and a further enhancement by assimilating T/P altimetry data into the solutions. The CSR tide models (3.0 and 4.0 versions) use the orthotide approach to model the residual tides of some preliminary hydrodynamic ocean-tide models using T/P altimeter data. From Table 3, it seems that NAO99b is the best model among the three. Using T/P SSHs, Chen (2001) found that the NAO99b tide model yields the smallest RMS crossover differences of SSH compared to the CSR4.0 and GOT99.2b tide models. Over shallow waters, all the collinear differences exceed 10 cm, translating to a 48-µrad (10^{-6}-radian) error in DOV of Geosat/GM. Even in the deep oceans, the collinear difference-implied DOV errors are still very large. Using available resources, we conducted a test over the SCS to compare the accuracies of predicted

Table 3. RMS collinear differences (in cm) of T/P (Matsumoto et al. 2000) and corresponding error (in µrad) in along-track DOV of Geosat/GM using different tide models

Tide model	$0 < H^a < 0.2$		$0.2 < H < 1$		$1 < H$	
	Difference	Error	Difference	Error	Difference	Error
NAO.99b	11.20	45	6.98	28	8.56	35
CSR4.0	15.77	64	7.37	30	8.55	35
GOT99.2b	13.99	57	7.37	30	8.65	35

[a] H = ocean depth in km

Table 4. RMS differences (in mGal) between shipborne and altimeter-derived gravity anomalies with different tide models

Tide model	ERS-1/GM	Geosat/GM (JGM3)
NAO99b	11.90	9.77
CSR3.0	11.93	not available
CSR4.0	not available	9.78

gravity anomalies using the CSR3.0, CSR4.0, and GOT99.2b tide models. As shown in Table 4, the NAO99b tide model produces the best accuracy in gravity anomaly. However, as can be seen from Table 4, the differences in accuracy are very close. This is partly due to the fact that DOV is insensitive to long-wavelength tide-model error. For Geosat/ERM, ERS-1/35d, ERS-2/35d, and T/P, the use of CSR3.0, CRS4.0, and NAO99b will probably not make too much difference because of the reduction of tide-model error by averaging data from repeat cycles.

3 Forming north and east components of DOV

3.1 Computing along-track DOV

The methods for computing MSSH and gravity anomaly in this paper will use DOV as the data type. By definition, an along-track DOV is the gradient of the geoid (with an opposite sign)

$$g = -\frac{\partial N}{\partial s} \quad (4)$$

where N is the geoid, which is a surface function, and s is the along-track distance. By this definition we would first need to construct a surface of the geoid and then perform a directional derivative along s to obtain DOV. Following this concept, we first fit a cubic spline (De Boor 1978) to the along-track geoidal heights from altimetry. Then the along-track derivative is obtained by differentiating the spline. The actual numerical computations were performed by the International Mathematical and Statistical Library (IMSL) routines. It turns out that such a procedure results in very noisy DOV, which is due to the interpolation error in fitting the spline. The interpolation error is particularly large when point spacings along a track segment are not uniform. Although this approach seems rigorous, it does not produce good results. A better result is obtained by simply approximating DOV by the slope of two successive geoidal heights

$$g \doteq -\frac{(N_2 - N_1)}{d} \quad (5)$$

where d is the point spacing. The geographic location of g is the mean location of the two geoidal heights. The estimated standard deviation of g is simply

$$\sigma_g = \frac{\sqrt{\sigma_1^2 + \sigma_2^2}}{d} \quad (6)$$

where σ_1 and σ_2 are the standard deviations of N_1 and N_2, respectively. In order to obtain geoidal height from SSH, both the time-dependent and quasi-time-independent SST values should be removed. In this paper, the time-dependent SST is reduced by filtering (see the discussion below), and for the quasi-time-independent SST we adopt the model of Levitus et al. (1997), which is available at NOAA's Ocean Climate Laboratory (see

http://www.nodc.noaa.gov/OC5/dyn.html). The Levitus SST values from NOAA are given as monthly averages on a $1° \times 1°$ grid for 12 months. We averaged the monthly values to obtain the required quasi-time-independent SST. Figure 2 shows the averaged Levitus SST, which looks very similar to the 1982 version of Levitus SST (cf. Hwang 1997, Fig. 3). The divided difference method (Gerald and Wheatley 1994) is then used to interpolate the required SST value from this SST grid at any altimeter data point.

3.2 Removing outliers and gridding DOV

Because of the use of a 1-D FFT algorithm in the computations of MSSH and gravity anomaly (see below), the north and east components of DOV need to be formed on regular grids with constant spacings in latitude and longitude. Before forming the regular grids, erroneous along-track DOV must be removed. Again we adopt Pope's tau-test method to remove possible outliers. Within a $4' \times 4'$ cell, any along-track DOV, ε_i, can form an observation equation as (cf. Heiskanen and Moritz 1985, p. 187)

$$\varepsilon_i + v_i = \xi \cos \alpha_i + \eta \sin \alpha_i, \quad i = 1, \ldots, n \qquad (7)$$

where v_i is the residual, α_i is the azimuth of ε_i, n is the number of points, and ξ and η are the north and east components. After LS estimating of ξ and η, all residuals in the $4' \times 4'$ cell can be determined using Eq. (7). A DOV is flagged as an outlier and is removed if its residual satisfies the condition

$$\frac{|v_i|}{\sigma_{v_i}} > \tau_c(m) \qquad (8)$$

where σ_{v_i} is the estimated standard deviation of v_i and $\tau_c(m)$ is the critical tau value at degree of freedom of m; see Koch (1987, p. 336) and Pope (1976) for the methods of computing σ_{v_i} and $\tau_c(m)$. Table 5 shows the ratios between removed and raw DOV in 12 selected areas. The removed DOV are largely from the non-repeat missions. In general, the removal ratios are relatively high in shallow waters and in higher latitudes, e.g. the Ross Sea, and low in the open ocean, e.g. the Reykjanes Ridge and the East Pacific Rise. One problem with the above procedure of outlier removal is that in areas with sparse data, such as coastal regions and polar regions, there are not enough data points to produce a large degree of freedom to make the result of the tau-test reliable, leading to undetected/improperly detected outliers.

After removing outliers the north and east components are then computed on a regular grid by the method of LSC (Moritz 1980)

$$\mathbf{s} = \begin{pmatrix} \xi \\ \eta \end{pmatrix} = \mathbf{C_{sl}}(\mathbf{C_{ll}} + \mathbf{C_n})^{-1}\mathbf{l} \qquad (9)$$

where vector $\mathbf{l}$ contains along-track DOV, vector $\mathbf{s}$ contains north (ξ) and east (η) components, $\mathbf{C_{sl}}$, $\mathbf{C_{ll}}$ and $\mathbf{C_n}$ are the covariance matrices for $\mathbf{s}$ and $\mathbf{l}$, $\mathbf{l}$ and $\mathbf{l}$, and the noise of $\mathbf{l}$, respectively. In Eq. (9), $\mathbf{C_n}$ is a diagonal matrix that in theory contains the variances of along-track DOV. When a reference gravity model is used, the error of the gravity model must be taken into account in constructing the covariance functions; see Hwang and Parsons (1995) and Hwang et al. (1998) for the methods of constructing the covariance functions when gridding DOV by LSC.

3.3 Selection of parameters

It turns out that many factors will affect the accuracies of altimeter-derived MSSH and gravity anomalies. Several parameters were tested in order to optimize the result. These parameters include a filter parameter and variances of SSHs from the non-repeat missions, and the searching radius (centered at a grid point) when gridding north and east components. For the non-repeat missions, filtering the raw, along-track SSHs can reduce the effect of sea surface variability and data noise. In the filtering, we choose to use the
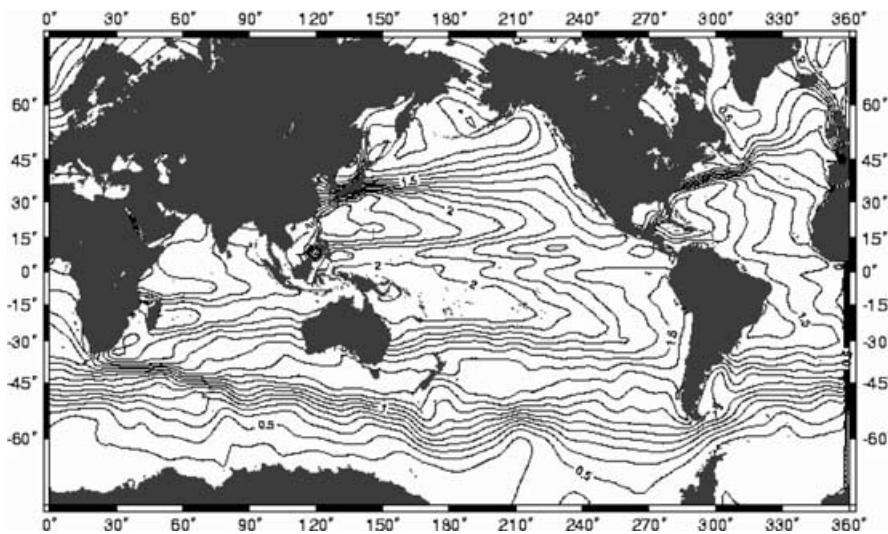

Fig. 2. Quasi-time-independent sea surface topography from Levitus et al. (1997); contour interval is 10 cm
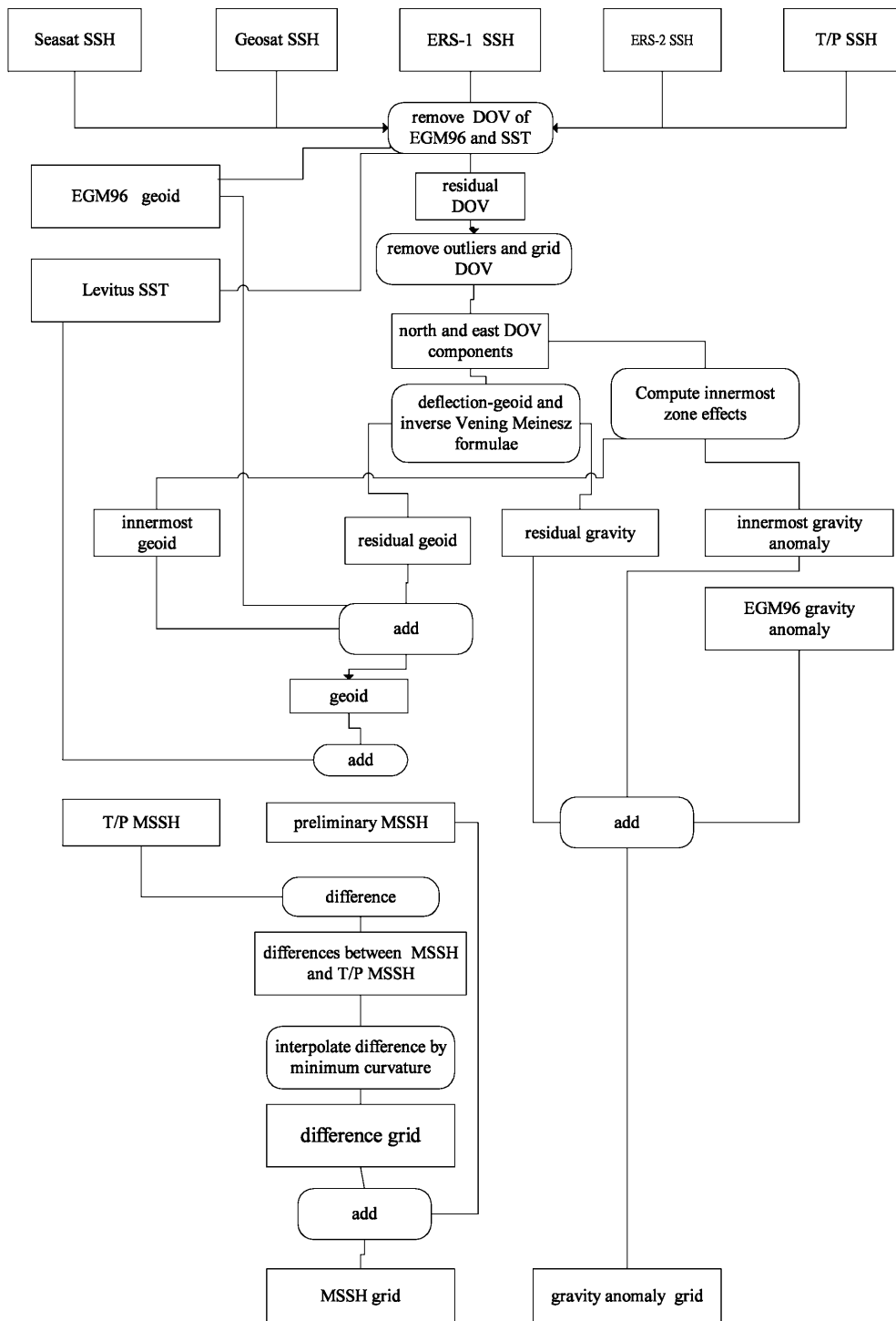
Fig. 3. Flowchart for computing global MSSH and gravity anomaly grids

Gaussian filter. The filter wavelength is the size of a window within which the raw SSHs are convolved with the Gaussian response function. The Gaussian response function has the form

$$r(x) = \exp(-\frac{x^2}{s^2}) \qquad (10)$$

where x is the distance between two data points and s is defined to be the filter parameter. The degree of smoothness increases with s. When filtering, all SSHs within a distance of $2s$ are used to convolve with the response function in Eq. (10) to obtain a filtered value. The filtered SSHs are then used to compute DOV in Eq. (5). Since filtering will lower the spatial resolution, we should compromise between noise/variability and smoothness. There is no need to filter the averaged SSHs from the repeat missions because the noise and sea surface variability have been reduced due to time averaging. As an example, Table 6 shows RMS differences between the predicted and shipborne gravity

Table 5. Test areas and ratios of removed outliers

Area	Geographic boundaries (latitude, longitude)	Total no. points	Deleted no. points	Ratio of outliers (%)
Alaska Abyssal	44° −61°, 99° −221°	696 082	27 224	3.9
East Pacific Rise	−26°–−9°, 229° −251°	809 120	27 474	3.4
Caribbean Sea	9° −31°, 269° −291°	609 605	29 404	4.8
Reykjanes Ridge	49° −66°, 319° −341°	800 624	29 949	3.7
Mediterranean Sea	−11° −11°, 339° −361°	855 408	28 254	3.3
Carlsberg Ridge	29° −46°, 0° −31°	202 545	17 506	8.6
Sierra Leone Basin	−1° −21°, 49° −71°	564 600	25 819	4.5
Kerguelen Plateau	−66°–−44°, 59° −81°	611 084	41 032	6.7
South China Sea	4° −26°, 104° −126°	495 338	27 478	5.5
Mariana Trench	4° −26°, 139° −161°	1 001 211	33 606	3.3
Fiji Plateau	−31° −9°, 159° −181°	982 678	33 875	3.4
Ross Sea	−71°–−59°, 199° −181°	458 505	38 042	8.2

Table 6. RMS differences between predicted and shipborne gravity anomalies using different filter parameters over the South China Sea

Filter parameter (km)			RMS difference (mGal)	
Seasat	ERS-1/GM	Geosat/GM	10°–20°N, 110°–120°E (deep ocean)	5°–25°N, 105°–125°E (deep, shallow oceans)
0	0	0	7.282	8.206
14	14	14	7.642	8.372
7	7	5	7.230	8.015
5	5	3.5	7.235	8.043

anomalies over the SCS using different choices of filter parameters. The comparisons were made in the deep-ocean part of the SCS and the whole of the SCS, the latter including the continental shelf. Indeed the result is improved with proper filtering, but will be degraded if SSHs are over-filtered. Based on the result in Table 6, we decided to use 7, 7, and 5 km as the filter parameters for Seasat, ERS-1/GM, and Geosat/GM, respectively.

Another issue is the variance of SSH and in turn the variance of DOV [see Eq. (6)] used in LSC. Based on the concept of collocation in the spectral domain and the concept of Wiener filtering, the degree of smoothness will increase with data variances (noises). For the repeat missions, the variances of the mean SSHs can be determined during averaging of the repeated measurements (see Table 2), which are automatically used in C_n of Eq. (9). For the non-repeat missions, we first tried to use the squared point SDs (see Fig. 1) as variances. Specifically, the variances of SSHs of Seasat and Geosat/GM are interpolated from the point variances that are derived from Geosat/ERM-derived point variances, and the variances of SSHs of ERS-1/GM are from ERS-1/35d-derived point variances. As seen in

Fig. 1, these point variances are relatively large compared to the predicted instrument noises of altimeters (cf. Seeber 1993). Using the point SDs in Fig. 1, the predicted gravity anomalies are very smooth and have very poor fit to the shipborne gravity anomalies. Because of this poor fit, we decided to use empirical SDs for the non-repeat missions. Table 7 shows the RMS differences between the predicted and shipborne gravity anomalies over the SCS based on different empirical SDs. For the three missions, the use of SD of 3–5 cm yields a better result compared to the case of using the SDs from the repeat mission. Based on the result in Table 7, we decided to use 5, 5, and 3.5 cm as the empirical SDs for Seasat, ERS-1/GM, and Geosat/GM, respectively.

The searching radius during gridding of DOV components will affect the accuracy of MSSH and gravity anomaly, as well as computational time. As an example, Table 8 shows the result of using different search radii in the SCS. The accuracy of predicted gravity anomaly increases with searching radius, but becomes stable after a certain radius. However, the computational time increases dramatically as the searching radius in-

Table 7. RMS differences between predicted and shipborne gravity anomalies using different point SDs of SSH over the South China Sea

Standard deviation			RMS difference (mGal)	
Seasat	ERS-1/GM	Geosat/GM	10°–20°N, 110°–120°E (deep ocean)	5°–25°N, 105°–125°E (deep, shallow oceans)
I[a]	I	I	8.345	9.142
5	5	3.5	7.230	8.015
5	3.5	3.5	7.461	8.075
5	5	2.5	7.323	8.037

[a] Interpolated from the point SDs of repeat missions

Table 8. Result of using different searching radii over the South China Sea

Radius	Difference between predicted and shipborne gravity anomalies (mGal)	CPU time[a] (s)
12′	7.230	1561
14′	7.098	5877
18′	7.026	16 699

[a] CPU time on a Pentium III 600 MHz running the SOLARIS OS

creases. Based on the result in Table 8, a radius of 14′ seems to be the best compromise between accuracy and computational time, thus this is our choice for computing the global grids.

4 Conversions from DOV to MSSH and gravity anomaly

We use the deflection-geoid and inverse Vening Meinesz formulae as the basic tool for computing MSSH and gravity anomaly. The deflection-geoid formula transforms DOV into geoidal height, which then yields MSSH by adding the quasi-time-independent SST. Detailed derivations of these two formulae are given in Hwang (1998). These two formulae read

$$\left\{ \begin{matrix} N_p \\ \Delta g_p \end{matrix} \right\} = \frac{1}{4\pi} \left\{ \begin{matrix} R \\ \gamma \end{matrix} \right\} \iint_\sigma (\xi_q \cos \alpha_{qp} + \eta_q \sin \alpha_{qp}) \left\{ \begin{matrix} C' \\ H' \end{matrix} \right\} \mathrm{d}\sigma_q$$

$$(11)$$

where

N_p = geoidal height at p (free index)
Δg_p = gravity anomaly at p
R = mean Earth radius; 6 371 000 m is used
γ = normal gravity, based on GRS80 (Torge 1989)
C', H' = Kernel functions
ξ_q, η_q = north and east components of DOV at q (dummy index)
α_{qp} = azimuth from q to p
σ = unit sphere
$\mathrm{d}\sigma_q$ = surface element = $\cos \phi_q \, \mathrm{d}\phi_q \, \mathrm{d}\lambda$; ϕ_q, λ_q are latitude and longitude

The kernel functions C' and H' are functions of spherical distance only and are defined in Hwang (1998). The 1-D FFT algorithm is used to rigorously implement Eq. (1). In the case of using a 360° reference field (see below), an optimal effective radius of integration in Eq. (11) is about 110 km (about 1° at the equator). In the 1-D FFT algorithm, all geoidal heights or gravity anomalies at a fixed latitude (or parallel) are computed simultaneously (Hwang 1998), and this is why the 1-D FFT algorithm is faster than the straight sum algorithm.

Because of the singularity of the kernel function C' and H' at zero spherical distance, the innermost zone effects on geoidal height and gravity anomaly must be taken into account and are computed by

$$\left\{ \begin{matrix} N_i \\ \Delta g_i \end{matrix} \right\} = \frac{1}{4} (\xi_y + \eta_x) \left\{ \begin{matrix} s_0^2 \\ 2s_0\gamma \end{matrix} \right\}$$

$$(12)$$

where $\xi_y = \partial\xi/\partial y$, $\eta_x = \partial\eta/\partial x$ (x is positive to the east and y is positive to the north), s_0 is the size of the innermost zone, which can be estimated from the grid intervals as

$$s_0 = \sqrt{\frac{\Delta x \Delta y}{\pi}}$$

$$(13)$$

Formulae such as those in Eq. (11) are based on spherical approximation. Errors arising from spherical approximation are investigated in detail by Moritz (1980). When using the remove–restore procedure (see below), the error in using spherical approximations should be very small compared to data noise. Consider the formula of error-free LSC in the case of using ellipsoidal correction (Moritz 1980, p. 328)

$$\mathbf{s} = \mathbf{C_{sl}} \mathbf{C_{ll}^{-1}} (\mathbf{l} - e^2 \mathbf{l^1}) + e^2 \mathbf{s^1}$$

$$(14)$$

where $\mathbf{s}, \mathbf{l}, \mathbf{C_{sl}}$ and $\mathbf{C_{ll}^{-1}}$ are defined in Eq. (9) and e^2 is the squared eccentricity of a reference ellipsoid, which is about 0.006694 for the GRS80 ellipsoid. The procedure in Eq. (14) is first to remove the ellipsoidal effect of the data, $e^2 \mathbf{l^1}$, then perform LSC computation, and finally add back the ellipsoidal effect of the signal $e^2 \mathbf{s^1}$. In the case of using the remove–restore procedure where a reference field is removed from the data and the residual signal is to be recovered, both $\mathbf{l^1}$ and $\mathbf{s^1}$ will be very small compared to their full signals [see Moritz (1980, p. 327), where the low-degree part will vanish due to the use of a reference field]. For example, if the largest element (DOV) in $\mathbf{l^1}$ is 100 μrad, then the largest element in $e^2 \mathbf{l^1}$ will be 0.66 μrad. This value is far smaller than the noise of DOV from the multi-satellite altimetry. Furthermore, if the largest element in $\mathbf{s^1}$ is 100 mGal, then the largest ellipsoidal effect on gravity anomaly is 0.66 mGal, which is much smaller than the error of the recovered gravity anomaly (see Tables 6–9). Of course, whether the reference field used in the remove–restore procedure will introduce additional error is another issue.

5 Global computation of mean sea surface and gravity anomaly grids

After the tests performed in the previous sections and the selection of a set of optimal parameters, MSSH and gravity anomalies on a $2' \times 2'$ grid were computed over the area $80°\text{S} - 80°\text{N}$ and $0° - 360°\text{E}$. The computations were divided into 36 areas, each covering a $40° \times 40°$

Table 9. RMS differences between predicted and shipborne gravity anomalies over the South China Sea with and without adding the innermost zone effect

Case	RMS difference (mGal)	
	10°–20°N, 110°–120°E	5°–25°N, 105°–125°E
With innermost zone	7.230	8.015
Without innermost zone	7.566	8.220

area. A batch job was created for each of the 36 areas and this batch job creates maps of altimeter data distribution, predicted MSSH and gravity anomaly, and many statistics for detailed examinations. The final global MSSH and gravity anomaly grids are a combination of the results from the 36 areas. Figure 3 shows the flowchart of computation in a $40° \times 40°$ area. The most time-consuming part in the procedure is the gridding of DOV. Only a few minutes of CPU time is needed for the 1-D FFT computation of geoid or gravity anomaly in a $40° \times 40°$ area on a Pentium III 600 machine. This computational procedure uses the EGM96 gravity model (Lemoine et al. 1998) to harmonic degree 360 as the reference field. In summary, reference DOV implied by EGM96 were removed from the raw DOV to yield residual DOV, which were used to compute residual geoidal heights and gravity anomalies using Eq. (11). The final geoidal heights and gravity anomalies are obtained by adding back the EGM96-implied values.

As seen in Fig. 3, the procedure for obtaining the global MSSH grid is more involved than that for the gravity anomaly grid. A preliminary MSSH grid was first obtained by adding the 1994 Levitus SST to the geoid grid. Because of the use of DOV as the data type, it is possible that the long-wavelength part of MSSH is lost in using the deflection-geoid formula. To mitigate such a loss, we first computed the differences between the along-track T/P, ERS-1 MSSH and the preliminary MSSH. Each difference is associated with a weight, which is the inverse of noise variance. Then smoothing and de-aliasing of the differences were carried out by computing the weighted median values within $15' \times 15'$ cells. The weighted median values were then interpolated on a $15' \times 15'$ grid using the minimum curvature method (Smith and Wessel 1990). The final MSSH grid is obtained by summing the difference grid (which is now re-sampled into a $2' \times 2'$ grid) and the preliminary grid. The resulting grids are now designated the NCTU01 MSSH grid and the NCTU01 gravity grid.

Because of the final adjustment using T/P MSSH, The SSH from the global MSSH grid is the height above a geocentric ellipsoid with a semi-major axis equal to 6 378 136.3 m and flattening equal to 1/298.257222101. The geodetic coordinates of both global grids are geodetic latitudes and longitudes defined by the T/P coordinate frame. In addition, the normal gravity for the global gravity anomaly grid is GRS80 because we have removed the zonal spherical harmonic coefficients C_{20}, C_{40}, C_{60}, and C_{80} of the GRS80 reference ellipsoid

(cf. Torge 1989) when computing the reference gravity anomalies from EGM96.

6 Model evaluations

6.1 The global MSSH grid

A standard method for evaluating an MSSH grid is to compare modeled MSSH and MSSH-derived gradients with averaged SSH and gradients from repeat missions. The first comparison is between the MSSH values from our model and those from repeat missions. Table 10 shows the result of the comparison of MSSH values using the averaged along-track SSH from T/P and ERS-1 (see Tables 1 and 2). Also included in Table 10 are the comparisons for the NASA/GSFC model (Wang 2000) and the CLS model (Hernandez and Schaeffer 2000). Compared to the NASA/GSFC and CLS models, the NCTU01 model agrees best with the T/P and the ERS-1 MSSH. The GSFC MSSH is slightly worse than the NCTU01 MSSH. On the continental shelves (depths below 200 m), all MSSH models contain large errors, which in the case of CLS have exceeded 20 cm. Even at median depths, the accuracy of MSSH is not very promising and is generally worse than 10 cm. All MSSH models have a best accuracy of a few centimeters in the deep oceans. The differences in the case of ERS-1 are smaller than in the case of T/P. This is to be explained by the fact that ERS-1 has a higher data density than T/P, so the former will dominate the resulting MSSH model. As such, the MSSH model will have a better match with ERS-1 SSH than T/P SSH. Furthermore, Fig. 4 shows the differences between the NCTU01 and T/P MSSH. Again the differences in Fig. 4 are large over shallow waters and small in the deep oceans. It is noted that the pattern of differences is very similar to the pattern of ocean variability in Fig. 1. This shows that the MSSH is less reliably determined in areas of high ocean variability than in other areas. Such a result agrees with the expected outcome of LS collocation [see Eq. (9)]: data with greater noise (variability) yield less reliable results.

Table 11 shows the RMS differences in gradients between the NCTU01, GSFC, and CLS modeled gradients and the averaged along-track gradients from T/P and ERS-1 missions. The NCTU01 and GSFC models have almost the same level of accuracy, while the CLS model has a slightly poorer accuracy than the other two. For all models the distribution of error is the same as

Table 10. RMS differences (in cm) between global sea surface models and T/P and ERS-1 MSSH

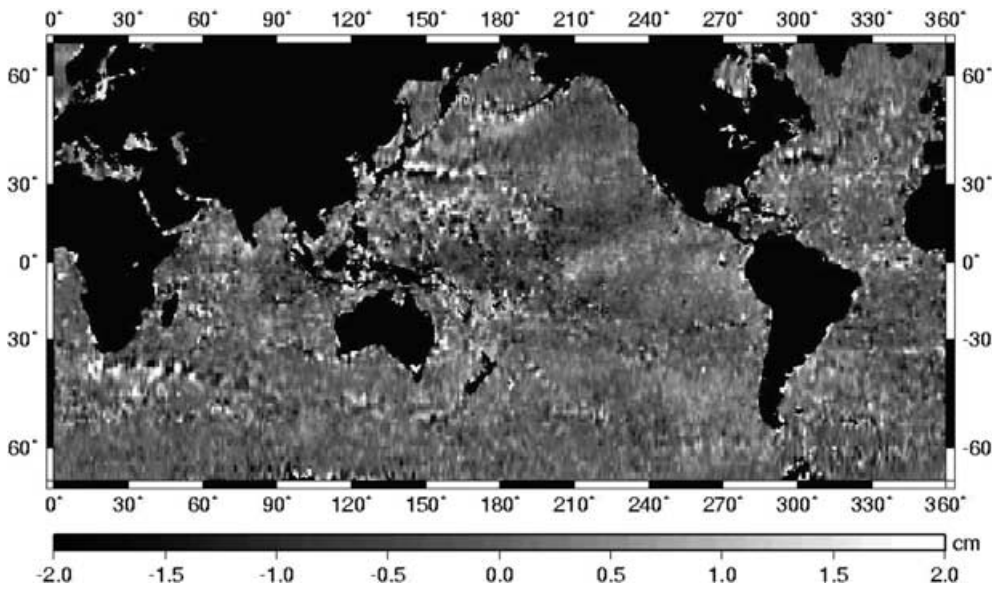|	T/P				ERS-1			
	0–0.2[a]	0.2–1	1–10	0–10	0–0.2	0.2–1	1–10	0–10
NCTU01	16.5	10.6	1.9	5.0	6.8	4.2	2.7	3.1
CLS	24.7	26.1	3.9	9.0	12.2	8.8	4.7	5.4
GSFC00	19.4	13.5	2.0	6.0	10.7	7.6	3.6	4.3
No. points	34 824	23 015	485 762	543 601	63 828	48 296	1 517 901	1 630 025

[a] Depths from 0 to 0.2 km

Fig. 4. Difference between NCTU01 and T/P mean SSHs

Table 11. RMS differences in along-track SSH gradients (in µrad) derived from global sea surface models and from T/P and ERS-1 MSSH

	T/P				ERS-1			
	0–0.2[a]	0.2–1	1–10	0–10	0–0.2	0.2–1	1–10	0–10
NCTU01	23.3	16.7	2.4	7.1	7.1	5.0	2.8	3.2
CLS	26.4	19.9	2.9	9.0	8.7	5.3	2.8	3.3
GSFC00	22.9	16.9	2.3	7.0	7.3	4.3	2.8	3.2
No. points	33 687	22 814	485 561	542 062	61 374	47 071	1 510 808	1 619 253

[a] Depths from 0 to 0.2 km

that of MSSH error, namely, bad accuracy over shallow waters and good accuracy in the deep oceans. Again, for the reason of data dominance, the error in the ERS-1 case is smaller than the error in the T/P case. In the T/P case the RMS difference of 7–9 µrad has far exceeded the standard deviation of T/P gradient, which is 1.9 µrad based on Eq. (6) (with an averaged point spacing of 6.6 km, see Table 2). On the other hand, in the ERS-1 case the RMS difference of 3.2 µrad agrees well with the expected standard deviation of 4.7 µrad of ERS-1 gradient (see Table 2).

6.2 The global gravity anomaly grid

In order to evaluate the accuracy of the NCTU01 gravity grid, we made a comparison between the predicted and shipborne gravity anomalies in 12 areas in the world's oceans (see Table 5 for the boundaries). These shipborne gravity data are from the National Geophysical Data Center. The corresponding ship tracks are shown in Fig. 5. The 12 areas are so selected that deep and shallow waters, and low and high latitudes are covered in the comparison. The comparison procedure and the adjustment of shipborne gravity data were detailed in Hwang et al. (1998). Briefly, long-wavelength biases in the shipborne gravity anomalies were first adjusted using altimetry-derived gravity

anomalies. A pointwise comparison was then made for the adjusted shipborne gravity anomalies. Table 12 shows the result of the comparison. In Table 12, the gravity grid from Hwang et al. (1998) is also compared. It has been shown that the gravity grid of Hwang et al. (1998) has a better accuracy than that of Sandwell and Smith (1997). As shown in Table 12, the accuracy of the current gravity grid has indeed improved over that of the gravity grid of Hwang et al. (1998). The improvement is most dramatic in the deep oceans such as the East Pacific Rise. In the Caribbean Sea, the improvement is also significant. Other areas with significant improvements are the Ross Sea and Kerguelen Plateau, which are situated in Antarctica. In general, the large difference between predicted and shipborne gravity anomalies may be due to either or both of the following reasons: (1) bad altimeter data quality, including data scarcity, and (2) large gravity signatures, for example in areas with trenches and seamounts. The largest differences, in the Fiji Plateau and then the Mediterranean Sea, can be attributed to the first reason. Due to possibly bad tide correction and contamination of altimeter waveforms by land mass and reefs, the predicted gravity anomalies in the Fiji Plateau are not expected to be of a good quality. A recent detailed analysis of errors in altimeter-derived gravity anomalies is given by Trimmer et al. (2001). In order to obtain a dramatic improvement of gravity
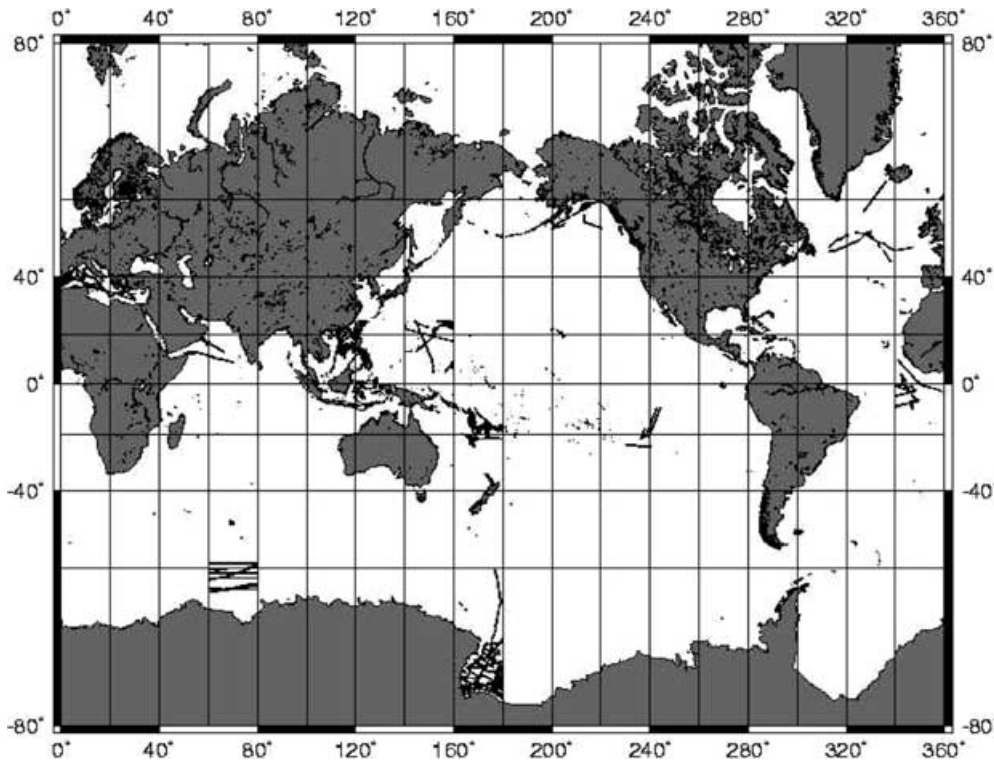
Fig. 5. Distributions of shipborne gravity anomalies in the 12 areas where the NCTU01 gravity anomaly grid is evaluated

Table 12. RMS differences (in mGal) between predicted and shipborne gravity anomalies in 12 areas

Comparison area	Present paper	Hwang et al. (1998)	Improvement
Alaska Abyssal	4.887	5.168	0.281
East Pacific Rise	3.057	6.786	3.729
Caribbean Sea	9.840	11.399	1.559
Reykjanes Ridge	5.122	5.202	0.080
Carlsberg Ridge	3.678	3.688	0.010
Mediterranean Sea	13.026	13.480	0.454
Sierra Leone Basin	7.347	7.397	0.023
Kerguelen Plateau	6.017	6.931	0.914
South China Sea	8.004	8.229	0.225
Mariana Trench	11.561	11.814	0.253
Fiji Plateau	13.365	14.148	0.783
Ross Sea	7.634	8.477	0.843

accuracy in such an area, a better tide model and improved determination of SSH by retracking altimeter waveforms will be needed. Improved SSHs by wave re-tracking have been reported in e.g. Anzenhofer and Shum (2001), Deng et al. (submitted), and Fairhead and Green (2001).

7 Conclusions

This paper describes the work of an improved computation of global MSSH and gravity anomaly grids using improved multi-satellite altimeter data sets and procedure. Various tests have been made in order to find an optimal set of parameters for the computation. The procedure is based on the deflection-geoid and inverse Vening Meinesz formulas, as well as the remove–restore concept. The crossover adjustment of SSHs is not used because of the use of DOV as the altimeter data type in the computation. Using DOV is particularly advantageous over areas with sparse altimeter data and in the case of long-wavelength error contained in altimeter data. The comparisons of the NCTU01 MSSH with the T/P and the ERS-1 MSSH result in overall RMS differences of 5.0 and 3.1 cm in SSH, respectively, and 7.1 and 3.2 μrad in SSH gradient, respectively. The agreements between the predicted and shipborne gravity anomalies range from 3.0 to 13.4 mGal, depending on the gravity signatures and the altimeter data noise, the latter being affected by instrument noise, sea state and accuracies of geophysical corrections. The NCTU01 MSSH model outperforms the NASA/GSFC model (Wang 2001) and the CLS model, and the NCTU01 gravity anomaly model has a better accuracy than those of the models of Sandwell and Smith (1997) and Hwang et al. (1998). The global MSSH and gravity grids will be posted in a public place for users to access.

References

Andersen O, Knudsen P (1998) Global marine gravity from the ERS-1 and Geosat geodetic mission altimetry. J Geophys Res 103: 8129–8137

Anzenhofer M, Shum CK (2001) Coastal altimetry and applications. Rep Department of Geodetic Science and Surveying, The Ohio State University, Columbus

Archiving, Validation, and Interpretation of Satellite Oceanographic Data (1996) AVISO user handbook for merged TOPEX/Poseidon products, 3rd edn. Toulouse, France

Bilitza D (1997) International reference ionosphere — status 1995/96. Adv Space Res 20(9): 1751–1754

Chen SA (2001) Determinations of tide, circulation and eddies over the South China Sea using TOPEX/POSEIDON altimeter data. PhD Thesis, National Chiao Tung University, Hsinchu, Taiwan

De Boor C (1978) A practical guide to splines. Springer, Berlin Heidelberg New York

Deng X, Featherstone WE, Hwang C, Berry PAM (submitted) Estimation of contamination of ERS-2 and POSEIDON satellite radar altimetry close to the coasts of Australia. Submitted to Mar Geod

Eanes R (1999) Improved ocean tide model from satellite altimetry. Fall Meeting 1999, Am Geophys Union, San Francisco

Fairhead JD, Green CM (2001) Pushing the resolution boundaries of marine satellite gravity. IAG 2001 Scientific Assembly, Budapest

Fu LL, Cazenave A (eds) (2001) Satellite altimetry and Earth sciences. Academic Press, New York

Gerald CF, Wheatley PO (1994) Applied numerical analysis, 5th edn. Addison-Wesley, New York

Heiskanen WA, Moritz H (1985) Physical geodesy. Reprint, Institute of Physical Geodesy, Tech Univ Graz, Austria

Hernandez F, Schaeffer P (2000) Altimetric mean sea surfaces and gravity anomaly maps inter-comparisons. AVI-NT-011-5242-CLS, CLS Ramonville St Agne

Hwang C (1997) Analysis of some systematic errors affecting altimeter-derived sea surface gradient with application to geoid determination over Taiwan. J Geod 71: 113–130

Hwang C (1998) Inverse Vening Meinesz formula and deflection-geoid formula: application to prediction of gravity and geoid over the South China Sea. J Geod 72: 304–312

Hwang C, Parsons B (1995) Gravity anomalies derived from Seasat, Geosat, ERS-1 and TOPEX/POSEIDON altimetry and ship gravity: a case study over the Reykjanes Ridge. Geophys J Int 122: 551–568

Hwang C, Kao EC, Parsons B (1998) Global derivation of marine gravity anomalies from Seasat, Geosat, ERS-1 and TOPEX/POSEIDON altimeter data. Geophys J Int 134: 449–459

Kalnay E, Kanamitsu M, Kistler R, Collins W, Deaven D, Gandin L, Iredell M, Saha S, White G, Woollen J, Zhu Y, Chelliah M, Ebisuzaki W, Higgins W, Janowiak J, Mo KC, Ropelewski C, Wang J, Leetmaa A, Reynolds R, Jenne R, Joseph D (1996) The NCEP/NCAR 40-year reanalysis project. Bull Am Meteol Soc 77: 437–471

Koch KR (1987) Parameter estimation in linear models. Springer, Berline Heidelberg New York

Le Traon PY, Ogor F (1998) ERS-1/2 orbit improvement using TOPEX/POSEIDON: the 2 cm challenge. J Geophys Res 103: 8045–8057

Lemoine FG, Kenyon SC, Factor JK, Trimmer RG, Pavlis NK, Chinn DS, Cox CM, Klosko SM, Luthcke SB, Torrence MH, Wang YM, Williamson RG, Pavlis EC, Rapp RH, Olson TR (1998) The development of joint NASA GSFC and the National Imagery and Mapping Agency (NIMA) geopotential model EGM96. Rep NASA/TP-1998-206861, National Aeronautics and Space Administration, Greenbelt, MD

Levitus S, Monterey GI, Boyer T (1997) Seasonal variability of dynamic height and its Fourier analysis. NOAA NESDIS Atlas 15, US Government Printing Office, Washington, DC

Liang CK (1983) The adjustment and combination of Geos-3 and Seasat altimeter data. Rep 346, Department of Geodetic Science and Surveying, The Ohio State University, Columbus

Matsumoto K, Takanezawa T, Ooe M (2000) Ocean tide models developed by assimilating TOPEX/POSEIDON altimeter data into hydrodynamical model: a global model and a regional model around Japan. J Oceanogr 56: 567–581

Matsumoto K, Sato T, Takanezawa T, Ooe M (2001) GOTIC2: a program for computation of oceanic tidal loading effect. J Geod Soc Jpn 47: 243–248

Moritz H (1980) Advanced physical geodesy. Herbert Wichmann, Karlsruhe

National Oceanic and Atmospheric Administration (1997) The complete Geosat altimeter GDR handbook. NODC Laboratory for Satellite Altimetry, Silver Spring, Md

Pope AJ (1976) The statistics of residual and the detection of outliers. Tech Rep TR-NOS-65-NGS-1, National Ocean Survey, Rockville, Md

Randel DL, VonderHaar TH, Ringerud MA, Stephens GL, Greenwald TJ, Combs CL (1996) A new global water vapor dataset. Bull Am Meteol Soc 77: 1233–1246

Rapp RH, Yi Y (1997) Role of ocean variability and dynamic ocean topography in the recovery of the mean sea surface and gravity anomalies from satellite altimeter data. J Geod 71: 617–629

Sandwell DT, Smith WHF (1997) Marine gravity anomaly from Geosat and ERS 1 satellite altimetry. J Geophys Res 102: 10 039–10 054

Schwarz KP, Sideris MG, Forsberg R (1990) The use of FFT techniques in physical geodesy. Geophys J Int 100: 485–514

Seeber G (1993) Satellite geodesy. De Gruyter, Berlin

Shum CK, Woodworth PL, Andersen OB, Egbert GD, Francies O, King C, Klosko SM, Le Provost C, Li X, Molines JM, Parke ME, Ray RD, Schlax MG, Stammer D, Tierney CC, Vincent P, Wunsch C (1997) Accuracy assessment of recent ocean tide models. J Geophys Res 102: 25 173–25 194

Smith WHF, Wessel P (1990) Gridding with continuous curvature splines in tension. Geophysics 55: 293–305

Torge W (1989) Gravimetry. De Gruyter, Berlin

Trimmer RG, Andersen O, Driscoll ML (2001) Estimating altimetry $5' \times 5'$ mean gravity anomaly regional accuracies. IAG 2001 scientific assembly, Budapest

Wang YM (2000) The satellite altimeter data derived mean sea surface GSFC98. Geophys Res Lett 27(5): 701–704

Yi Y (1995) Determination of gridded mean sea surface from TOPEX, ERS-1 and GEOSAT altimeter data. Rep 434, Department of Geodetic Science and Surveying, The Ohio State University, Columbus